MoS$_2$/MnO$_2$ heterostructured nanodevices for electro-chemical energy storage

Xiaobin Liao[1], Yunlong Zhao[1,2], Junhui Wang[1], Wei Yang[1], Lin Xu[1], Xiaocong Tian[1], Yi Shuang[1], Kwadwo Asare Owusu[1], Mengyu Yan[1] (✉), and Liqiang Mai[1,3] (✉)

[1] *State Key Laboratory of Advanced Technology for Materials Synthesis and Processing, Wuhan University of Technology, Wuhan 430070, China*

[2] *Department of Chemistry and Chemical Biology, Harvard University, Cambridge, Massachusetts 02138, USA*

[3] *Department of Chemistry, University of California, Berkeley, California 94720, USA*

ABSTRACT

Hybrid or composite heterostructured electrode materials have been widely studied for their potential application in electrochemical energy storage. Whereas their physical or chemical properties could be affected significantly by modulating the heterogeneous interface, the underlying mechanisms are not yet fully understood. In this work, we fabricated an electrochemical energy storage device with a MoS$_2$ nanosheet/MnO$_2$ nanowire heterostructure and designed two charge/discharge channels to study the effect of the heterogeneous interface on the energy storage performances. Electrochemical measurements show that a capacity improvement of over 50% is achieved when the metal current collector was in contact with the MnO$_2$ instead of the MoS$_2$ side. We propose that this enhancement is due to the unidirectional conductivity of the MoS$_2$/MnO$_2$ heterogeneous interface, resulting from the unimpeded electrical transport in the MnO$_2$-MoS$_2$ channel along with the blocking effect on the electron transport in the MoS$_2$-MnO$_2$ channel, which leads to reaction kinetics optimization. The present study thus provides important insights that will improve our understanding of heterostructured electrode materials for electrochemical energy storage.

1 Introduction

Electrochemical energy storage devices with high energy density are urgently needed for the electronics, electric vehicles, and power industries [1]. Significant efforts have been focused on optimizing the properties of electrode materials in order to achieve higher energy densities. An effective strategy involves the development of core–shell [2–6], branched [7–10], and axial heterostructures [11–14]. The physical or chemical properties of these systems could be affected significantly by modulating the heterogeneous interface.

Address correspondence to Liqiang Mai, mlq518@whut.edu.cn; Mengyu Yan, ymymiles@whut.edu.cn

However, the underlying mechanisms are not yet fully understood, due to the multicomponent nature and complex structure of batteries and electrode materials.

Nanoscale devices have been widely applied as nanoprobes for real-time, highly sensitive, and label-free detection in sensors and medical applications [15, 16]. For energy storage applications, nanoscale electrochemical devices with compact circuit size could help revealing the underlying mechanisms of electrode materials, by *ex/in situ* probing electrical transport in the electrode material during charge/discharge processes [17–20]. For example, Feng and coworkers designed an electrochemical device to study the physical and chemical properties of nanoscale MoS_2 by electro-chemically inserting Li^+ ions in the interlayer spacing of MoS_2. Our group designed a single nanowire-based battery to investigate the capacity fading mechanisms; using *in situ* electrical transport measurements, we found that the capacity fading is related to the intrinsic conductance decay of the electrode material [21–24]. Therefore, the fabrication of heterostructured nanoscale energy storage devices represents an effective approach to study the electrochemical behaviors and intrinsic mechanisms of heterostructured systems.

Two-dimensional (2D) transition metal dichalcogenide (TMDC) materials such as layered MoS_2 have been widely studied for energy storage applications, owing to their unique structure and excellent electrical conductivity; however, the applications of these materials are limited by their low energy density [25–29]. To address this issue, the fabrication of heterostructured materials combining MoS_2 with other components with higher capacity density has been extensively investigated [11, 30, 31]. Typical one-dimensional metal oxides such as MnO_2 nanowires have received considerable interest for energy storage applications due to their higher capacity density, despite their poor electrical conductivity. Many studies have demons-trated that the electrochemical performances of MnO_2 nanowires can be improved by fabricating heteros-tructures with 2D materials, in order to modify the electrical conductivity [32–36]. However, as these reports mainly focused on the design of heterostructured materials, the fundamental physical and chemical relationships between electrochemical performances and heterostructure are still unclear. In this work, we deposited layered MoS_2 nanosheet on single MnO_2 nanowire to fabricate a MoS_2/MnO_2 heterostructured electrochemical energy storage device, and investigated its electrical transport and electrochemical properties to understand how the heterogeneous interface could affect the energy storage performances by modulating the testing modes (Figs. 1(a) and 1(b)).

2   Experimental

2.1   Synthesis of MnO_2 nanowires

Pure MnO_2 nanowires were synthesized by a hydro-thermal method. In a typical synthesis, 2 mmol of $KMnO_4$ and 2 mmol of NH_4F were added to 80 mL of distilled water and magnetically stirred at room
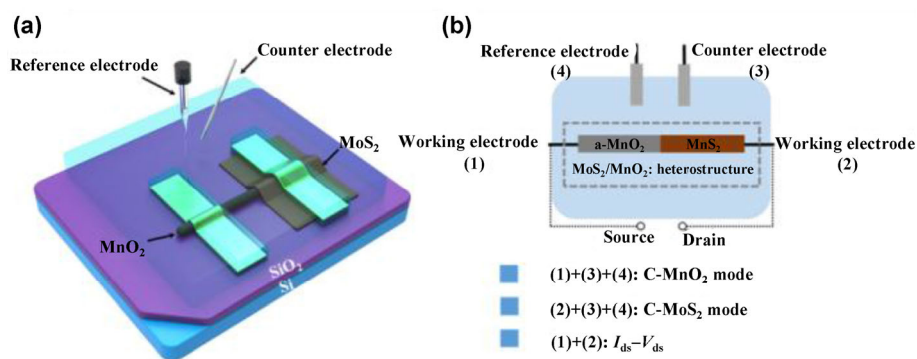
Figure 1 MoS_2/MnO_2 heterostructured energy storage device. (a) Schematic illustration of the MoS_2/MnO_2 heterostructured energy storage device. Two working electrodes (1) and (2) are separately connected to the layered MoS_2 nanosheet and single MnO_2 nanowire. Ag/AgCl and a Pt wire serve as reference electrode (4) and counter electrode (3), respectively. A 6 M KOH solution is used as the electrolyte. (b) Illustration of the testing modes for the MoS_2/MnO_2 heterostructured energy storage device.

temperature for 1 h. The solution was then placed into a 100-mL autoclave and heated at 180 °C for 48 h. The sample was then washed and dried, and a black powder was obtained.

2.2 Fabrication of heterostructured MoS$_2$ nanosheet/MnO$_2$ nanowire-based energy storage devices

For the fabrication of silicon wafers with outer electrodes, LOR 3A and S1805 photoresists were first coated on silicon wafers (with a 300 nm SiO$_2$ layer) by spin coating. The silicon wafers were then exposed to ultraviolet light for 1.5 s, and the patterned silicon wafers were obtained after developing and rinsing. Next, 5 nm Cr and 50 nm Au were deposited on the silicon wafers by thermal evaporation. The silicon wafers patterned with the 5 nm Cr/50 nm Au outer electrodes were then obtained after removing the photoresists with acetone.

MnO$_2$ nanowires were transferred onto the prepared silicon wafers by spin coating, followed by stacking the layered MoS$_2$ nanosheets (obtained through micromechanical exfoliation) on the MnO$_2$ nanowires using scotch tape. Then, Cr/Au (5 nm/150 nm) contacts acting as source and drain were designed and deposited by electron beam lithography and thermal evaporation. After lift-off, the Cr/Au contacts were passivated by a SU-8 layer to avoid leakage currents between the Pt counter electrode and the Cr/Au contacts. Finally, a 6 M KOH electrolyte was dropped onto the energy storage device to cover the MoS$_2$/MnO$_2$ heterostructure. An Ag/AgCl electrode was used as the reference electrode (Fig. S1 in the Electronic Supplementary Material (ESM)).

2.3 Characterization

Scanning electron microscopy (SEM) images of the devices were obtained with a FESEM JSM-7001F microscope at an acceleration voltage of 20 kV. Raman spectra were recorded using a Renishaw RM-1000 laser Raman microscope with 632.8 nm excitation light source. Atomic force microscopy (AFM) measurements were performed with a Bruker MultiMode VIII instrument. An Autolab 302N probe station (Lake Shore, TTPX) and a semiconductor device analyzer (B1500A) were used to test the electrical conductivity characteristics and electrochemical performances of the devices.

3 Results and discussion

Figure S2 (in the ESM) shows the optical and SEM images, along with an illustration of the energy storage device. Figure 2(a) and Fig. S2(d) in the ESM display SEM images of the MoS$_2$/MnO$_2$ heterostructure, which show that the MoS$_2$ nanosheet overlaps with the MnO$_2$ nanowire. The cross-sectional image highlights the overall integration of the MnO$_2$-MoS$_2$-Cr/Au contacts vertical stack in the MoS$_2$/MnO$_2$ heterostructure (Fig. S2(e) in the ESM). The total channel area is defined by the exposed area of the MoS$_2$/MnO$_2$ electrode material. The testing instruments include an electrochemical workstation and a semiconductor device analyzer. The electrochemical workstation is mainly used to measure the electrochemical performances of the MoS$_2$/MnO$_2$ heterostructured electrode. The electrical transport characteristics of the MoS$_2$/MnO$_2$ heterostructure can be measured accurately by the semiconductor device analyzer.

Raman spectroscopy measurements were carried out to determine the structure of the layered MoS$_2$, MnO$_2$ nanowire, and MoS$_2$/MnO$_2$ heterostructure. The Raman spectra of these materials were recorded with a 632.8 nm excitation light source. Different regions of the MoS$_2$/MnO$_2$ heterostructure were irradiated with the Raman light (Fig. 2(a)), in order to determine the Raman characteristics of the layered MoS$_2$ nanosheet (Fig. 2(b)), MnO$_2$ nanowire (Fig. 2(c)), and MoS$_2$/MnO$_2$ heterostructure (Fig. 2(d)). The layered MoS$_2$ obtained by physical exfoliation shows Raman peaks at 143, 178, 377, 408, 418, 459, 526, 569, 595, 640, 761, 779, and 819 cm^{-1}, which include the typical E$^1_{2g}$ (143 cm^{-1}), E$^1_{2g}$ (377 cm^{-1}), and A$_{1g}$ (408 cm^{-1}) peaks, consistent with previous studies [37–40]. The MnO$_2$ nanowire exhibits Raman peaks at 181, 298, and 617 cm^{-1}, corresponding to the O–Mn–O and Mn–O modes [41–43]. Importantly, no extra peaks are found in the Raman spectrum of the MoS$_2$/MnO$_2$ heterostructure, compared with the spectra of the MnO$_2$ nanowire and layered MoS$_2$. This indicates that no new chemical bonds are generated at the contact interface of the MoS$_2$/MnO$_2$ heterostructure upon vertically stacking the layered MoS$_2$
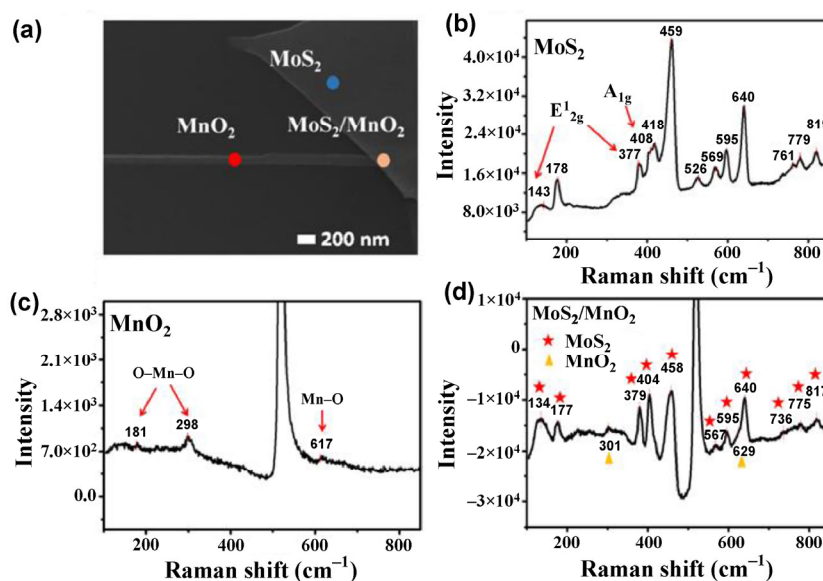
Figure 2 Structural characterization of the MoS_2/MnO_2 heterostructured energy storage device. (a) SEM image of the MoS_2 nanosheet (marked with a blue spot), MnO_2 nanowire (red spot), and MoS_2/MnO_2 heterostructure (pink spot); (b)–(d) Raman spectra of layered MoS_2 nanosheet (b), MnO_2 nanowire (c), and MoS_2/MnO_2 heterostructure (d).

nanosheet on the MnO_2 nanowire by physical means.

The vertically stacked architecture of the MoS_2/MnO_2 heterostructure was further confirmed by AFM. The AFM image in Fig. S3(a) in the ESM shows that the layered MoS_2 is covered on one end of the MnO_2 nanowire. The height profile of the MoS_2/MnO_2 heterostructure (Fig. S3(b) in the ESM) indicates that the thicknesses of the exfoliated layered MoS_2 (red line) and MnO_2 nanowire (green line) are about 37 and 25 nm, respectively. On the other hand, the thickness of the layered MoS_2 and MnO_2 nanowire in the overlapping region is ~70 nm. Moreover, the diameter of the MnO_2 nanowire is ~200 nm. The exposed area of the MoS_2/MnO_2 electrode material is ~8.3 μm^2, which is used to define the effective area in further calculations.

To study how the heterogeneous interface affects the energy storage performance, the charge/discharge processes of the MoS_2/MnO_2 heterostructured nanodevice were carried out in the MnO_2-MoS_2 (denoted as C-MnO_2 mode, current collector in contact with the MnO_2 side) and MoS_2-MnO_2 (denoted as C-MoS_2 mode, current collector in contact with the MoS_2 side) channels (Fig. 3(a)). To avoid the hydrogen evolution and oxygen reduction reactions, we selected a potential

range between −0.2 and 0.4 V vs. Ag/AgCl for the electrochemical measurements in a three-electrode system (Figs. S4–S6 in the ESM). First, we measured the cyclic voltammetry (CV) curves of the MoS_2/MnO_2 heterostructure under different modes (Fig. 3(b)). The capacity of the electrode material was calculated using the following equation [44]

$$C = \frac{\int IdV}{2 \times S \times A \times \Delta V} \tag{1}$$

where I, S, A, and ΔV represent the working current, scanning rate, exposed area of the electrode material, and voltage window, respectively. The calculated capacities are shown in Fig. 3(c). Notably, under the C-MnO_2 mode, the MoS_2/MnO_2 heterostructure can deliver a capacity of 0.31 mAh·cm^{-2} at a scan rate of 20 mV·s^{-1}, which is almost 55% higher than that recorder under the C-MoS_2 mode (0.20 mAh·cm^{-2}). Similar results were obtained at different scan rates (Fig. 3(c)). We also evaluated the cycling performances of the MoS_2/MnO_2 heterostructure under the C-MnO_2 and C-MoS_2 modes. The MoS_2/MnO_2 heterostructure delivered a higher reversible capacity under the C-MnO_2 than C-MoS_2 mode after 50 cycles at 100 mV·s^{-1} (Fig. S7 in the ESM).
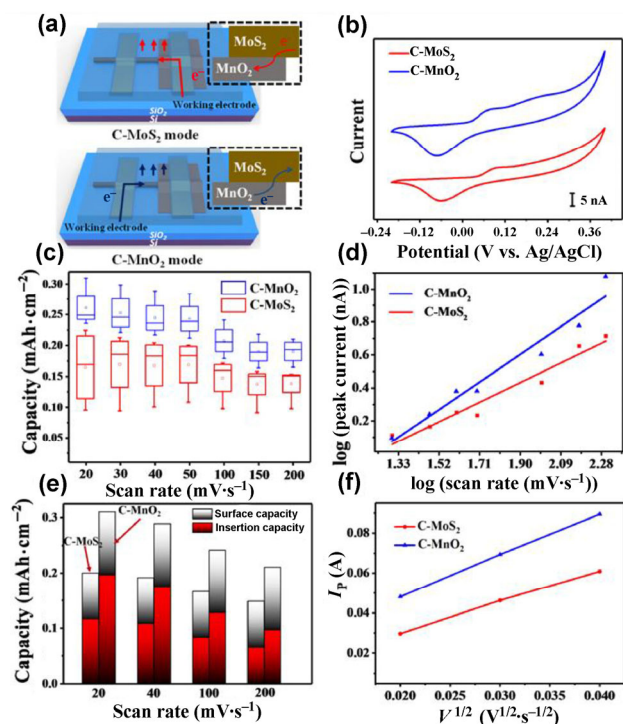
Figure 3 Electrochemical performance and kinetic analysis of the MoS_2/MnO_2 heterostructure. (a) Schematic illustration of the different measuring modes of the MoS_2/MnO_2 heterostructure; (b) CV curves of the MoS_2/MnO_2 heterostructure scanned at 20 mV·s^{-1} under different modes in 6 M KOH; (c) specific capacity of the MoS_2/MnO_2 heterostructure under different modes with scan rate varying from 20 to 200 mV·s^{-1}; (d) b-value analysis of the MoS_2/MnO_2 heterostructure under different modes; (e) surface and insertion capacity contributions of the MoS_2/MnO_2 heterostructure at different scan rates; (f) ion diffusion coefficients of the MoS_2/MnO_2 heterostructure calculated by the Randles–Sevick equation.

To investigate the kinetic processes under different modes, we calculated the b value of the MoS_2/MnO_2 heterostructure according to Eq. (2) [45]

$$i = av^b \tag{2}$$

where i is the current, a is a constant, v is the scan rate, and b represents the capacitive and diffusion contribution to the current obtained from a power fit of the current vs. scan rate plot. A b value of 0.5 indicates that the current is limited by the semi-infinite diffusion, whereas a value of 1 means that the current is surface-controlled. The b values of the MoS_2/MnO_2 heterostructure under the C-MoS_2 and C-MnO_2 modes, calculated from the plots in Fig. 3(d), were 0.62 and 0.69, respectively, for scan rates ranging

from 20 to 200 mV·s^{-1}. The b values of the MoS_2/MnO_2 heterostructure under different modes are close to 0.5, which indicates that the kinetic behaviors of the MoS_2/MnO_2 heterostructure under different modes are similar and mainly controlled by diffusion processes.

To investigate the capacity contribution, we calculated the surface and insertion capacities of the MoS_2/MnO_2 heterostructure at different scan rates. The current response i at a fixed potential V can be described as the sum of two contributions corresponding to the surface and intercalation capacities, as discussed below [46, 47]

$$i(V) = k_1 v + k_2 v^{1/2} \tag{3}$$

or

$$i(V) / v^{1/2} = k_1 v^{1/2} + k_2 \tag{4}$$

where v represents the scan rate, while $k_1 v$ and $k_2 v^{1/2}$ denote the current contributions from the surface capacity (surface pseudocapacity and double-layer capacity) and insertion processes (insertion pseudo-capacity), respectively. By determining k_1 and k_2, it is possible to distinguish the fractions of current arising from the surface capacity and insertion processes at a specific potential. As shown in Fig. 3(e), with increasing scan rate, the capacities of the MoS_2/MnO_2 heterostructure under C-MoS_2 and C-MnO_2 modes decrease congruously. This reflects the fact that higher scan rates limit the ion diffusion process, which prevents the ions from accessing the MoS_2/MnO_2 heterostructure. Therefore, at high scan rates the surface capacity of the electrode materials becomes the main source of total capacity [48]. The surface capacity of the MoS_2/MnO_2 heterostructure under the C-MoS_2 mode is 0.084 mAh·cm^{-2}, which represents 42% of the total capacity (0.200 mAh·cm^{-2}) at 20 mV·s^{-1}. Moreover, the surface capacity of the MoS_2/MnO_2 heterostructure under the C-MnO_2 mode is 0.114 mAh·cm^{-2}, which accounts for 37% of the total capacity (0.310 mAh·cm^{-2}) at 20 mV·s^{-1}. The surface capacity fractions of the MoS_2/MnO_2 heterostructure under the C-MoS_2 mode are 44%, 50%, and 57% (to be compared with 40%, 47%, and 54% for the C-MnO_2 mode) at scan rates of 40, 100, and 200 mV·s^{-1}, respectively. Figure S8 in the ESM compares the surface capacity (shaded region) and total current obtained at a scan rate of 100 mV·s^{-1}

for the MoS_2/MnO_2 heterostructure under the C-MoS_2 and C-MnO_2 modes. At scan rates of 20–200 mV·s^{-1}, the fraction of insertion capacity is higher under the C-MnO_2 mode than under the C-MoS_2 mode. These results can be explained by the *b*-value analysis of the MoS_2/MnO_2 heterostructure, which indicates that the kinetic behavior of the MoS_2/MnO_2 heterostructure is mainly controlled by diffusion processes. Most importantly, the surface and insertion capacities of the MoS_2/MnO_2 heterostructure under the C-MnO_2 mode are both higher than those measured under the C-MoS_2 mode.

For a better understanding of these effects, we calculated the ionic diffusion coefficients of the MoS_2/MnO_2 heterostructure under C-MnO_2 and C-MoS_2 modes. In order to study the ionic transport in the MoS_2/MnO_2 heterostructured energy storage device, the apparent diffusion coefficients were calculated via the Randles–Sevick equation [49]

$$I_p = 0.4463 n \times FAC \left(\frac{NFvD}{RT} \right)^{1/2}$$
$$= [269000 \times n^{3/2} A D^{1/2} C] v^{1/2} \qquad (5)$$

where I_p is the peak current, n is the number of electrons transferred per molecule during the electrochemical reaction (1 in this case), A is the exposed area of the electrode material, C is the concentration of potassium ions in the electrolyte (6 M in the present system), D is the ionic diffusion coefficient of the whole electrode, reflecting the diffusion of both potassium and hydroxyl ions, and v is the scanning rate. The detailed information is shown in Fig. 3(f). The calculated ionic diffusion coefficient of the MoS_2/MnO_2 heterostructure under the C-MnO_2 mode is 1.28×10^{-5} cm^2·s^{-1}, which is almost 1.3 times as high as that measured under the C-MoS_2 mode (9.68×10^{-6} cm^2·s^{-1}). These results indicate that the MoS_2/MnO_2 heterostructure exhibits a higher ionic diffusion rate, resulting in enhanced storage capacity under the C-MnO_2 mode.

The MoS_2/MnO_2 heterostructure exhibits different capacity and ionic diffusion properties under C-MnO_2 and C-MoS_2 modes. In order to explain this finding, we further examined the electrical transport characteristics of the MoS_2/MnO_2 heterostructure. The *I–V* curves of the layered MoS_2 and MoS_2/MnO_2 heteros-

tructure are shown in Figs. 4(a) and 4(b), respectively. The MoS_2/MnO_2 heterostructure displays unidirectional conductivity and achieves an on/off ratio of 10^4 with a low leakage current, down to 1×10^{-11} A (Fig. 4(c)). The unidirectional conductivity can be explained by the semiconductor device theory: Layered MoS_2 is an n-type material and its main charge carriers are free electrons [50, 51]. On the other hand, MnO_2 is a p-type material and its main charge carriers are holes (as can be proved from the results in Fig. 4(b)) [52–55]. When these two different types of materials are connected, the free carriers (electrons and holes) interpenetrate each other and combine at the interface for the concentration difference, which results in negative MnO_2 and positive MoS_2 regions at the heterogeneous interface (Fig. 4(d)). According to the p–n junction theory [56], the electrons in the MnO_2/MoS_2 heterostructure can transfer freely from MnO_2 to MoS_2 (corresponding to the C-MnO_2 mode). However, the electron transfer process is hampered along the MoS_2 to MnO_2 direction (corresponding to the C-MoS_2 mode). The blocking effect on the electrons transfer process might be the main reason for the 55% higher capacity of the MnO_2/MoS_2 heterostructure under C-MnO_2 than C-MoS_2 mode.

In situ measurements of electrical transport in the MnO_2/MoS_2 heterostructure were performed to understand how the unidirectional conductivity influences the electrochemical properties of the MoS_2/MnO_2 heterostructure during the charge/discharge processes. *I–V* plots were obtained under dry conditions in order to avoid any influence from the electrolyte. The *I–V* plot of the MoS_2/MnO_2 heterostructure after discharge is shown in Fig. 5(a). The MoS_2/MnO_2 heterostructure shows a bidirectional conductivity after the discharge process, which can be understood by assuming that the insertion of ions results in the breakup of the blocking effect at the heterogeneous interface. As a result, electron transfer can take place across the interface of the MoS_2/MnO_2 heterostructure during the discharge processes under both C-MnO_2 and C-MoS_2 modes. After the first charge/discharge cycle, the MoS_2/MnO_2 heterostructure exhibits unidirectional conductivity again (Fig. 5(b)). After several cycles, a few number of ions are captured by the MoS_2/MnO_2 heterostructure and the on/off ratio
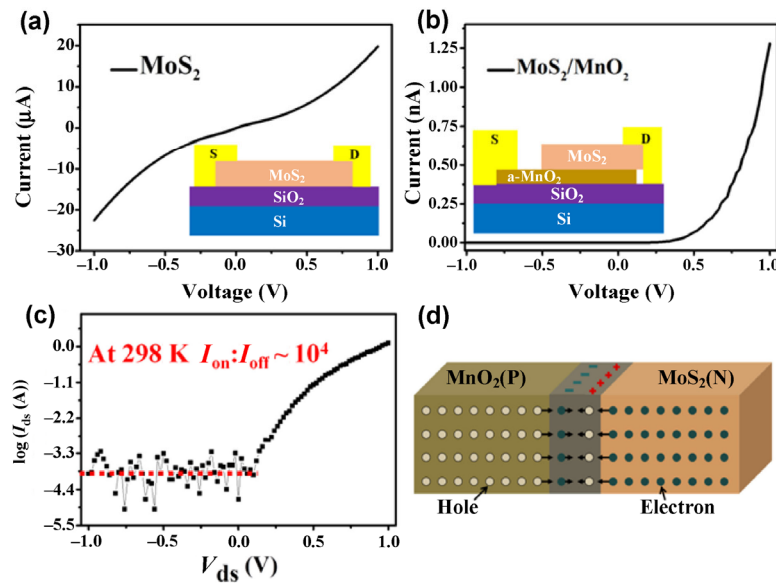
Figure 4 Electrical transport characteristics of layered MoS_2 and MoS_2/MnO_2 heterostructure without electrolyte. (a) $I–V$ curve of layered MoS_2; (b) $I–V$ curve of MoS_2/MnO_2 heterostructure; (c) on/off ratio of MnO_2/MoS_2 heterostructure; (d) distribution of electrons and holes in the MoS_2/MnO_2 heterostructure.
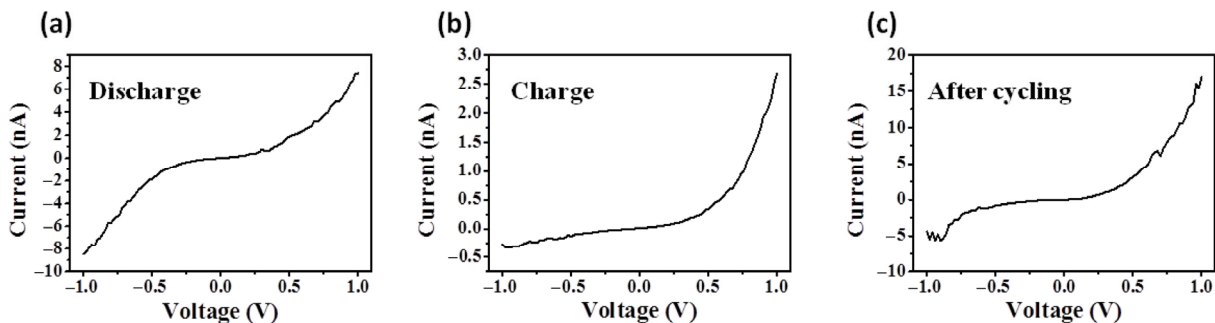
Figure 5 *In situ* electrical transport measurements during charge/discharge processes in MoS_2/MnO_2 heterostructure. (a) $I–V$ curve of MoS_2/MnO_2 heterostructure after the discharge process. The MoS_2/MnO_2 heterostructure shows a bidirectional conductivity. (b) $I–V$ curve of MoS_2/MnO_2 heterostructure after the charge process. The heterostructure regains unidirectional conductivity, and the on/off ratio shows a slight decrease. (c) $I–V$ curve of MoS_2/MnO_2 heterostructure after several cycles.

declines visibly and permanently (Fig. 5(c)). Under the C-MnO_2 mode, electron transport can take place in the electrode material during both charge and discharge processes. However, under the C-MoS_2 mode, the electrical transport in the electrode material is hampered during the charge process, which results in loss of capacity of the MnO_2/MoS_2 heterostructure.

4   Conclusions

In the present work, we investigated an energy storage device based on a MoS_2 nanosheet/MnO_2 nanowire heterostructure and revealed that the unidirectional conductivity of the heterogeneous interface could significantly affect its energy storage performances. Electrical transport in the MnO_2-MoS_2 channel can proceed unimpeded during both charge and discharge processes. However, electrical transport in the MoS_2-MnO_2 channels is hampered during the charge process, which results in loss of capacity of the MnO_2/MoS_2 heterostructure. The results presented here can guide the design of new heterostructured electrode materials and provide an important platform for understanding the fundamental relationships between the electrical transport characteristics and the electrochemical performances of heterostructured materials.

Acknowledgements

Electronic Supplementary Material: Supplementary material (illustration of the fabrication processes of the energy storage device, optical image of the outer electrodes, SEM image, AFM image and CV curves of the MoS_2/MnO_2 heterostructure) is available in the online version of this article at https://doi.org/10.1007/s12274-017-1826-6.

References

[1] Palacín, M. R.; De Guibert, A. Why do batteries fail? *Science* **2016**, *351*, 1253292.

[2] Xia, X. H.; Tu, J. P.; Zhang, Y. Q.; Wang, X. L.; Gu, C. D.; Zhao, X. B.; Fan, H. J. High-quality metal oxide core/shell nanowire arrays on conductive substrates for electrochemical energy storage. *ACS Nano* **2012**, *6*, 5531–5538.

[3] Xiong, Q. Q.; Tu, J. P.; Xia, X. H.; Zhao, X. Y.; Gu, C. D.; Wang, X. L. A three-dimensional hierarchical Fe_2O_3@NiO core/shell nanorod array on carbon cloth: A new class of anode for high-performance lithium-ion batteries. *Nanoscale* **2013**, *5*, 7906–7912.

[4] Asakura, D.; Li, C. H.; Mizuno, Y.; Okubo, M.; Zhou, H. S.; Talham, D. R. Bimetallic cyanide-bridged coordination polymers as lithium ion cathode materials: Core@shell nanoparticles with enhanced cyclability. *J. Am. Chem. Soc.* **2013**, *135*, 2793–2799.

[5] Kim, D. W.; Hwang, I. S.; Kwon, S. J.; Kang, H. Y.; Park, K. S.; Choi, Y. J.; Choi, K. J.; Park, J. G. Highly conductive coaxial SnO_2-In_2O_3 heterostructured nanowires for Li ion battery electrodes. *Nano Lett.* **2007**, *7*, 3041–3045.

[6] Peng, P.; Milliron, D. J.; Hughes, S. M.; Johnson, J. C.; Alivisatos, A. P.; Saykally, R. J. Femtosecond spectroscopy of carrier relaxation dynamics in type II CdSe/CdTe tetrapod heteronanostructures. *Nano Lett.* **2005**, *5*, 1809–1813.

[7] Zhou, W. W.; Cheng, C. W.; Liu, J. P.; Tay, Y. Y.; Jiang, J.; Jia, X. T.; Zhang, J. X.; Gong, H.; Hng, H. H.; Yu, T. et al. Epitaxial growth of branched α-Fe_2O_3/SnO_2 nano-heterostructures with improved lithium-ion battery performance. *Adv. Funct. Mater.* **2011**, *21*, 2439–2445.

[8] Zhou, S.; Liu, X. H.; Wang, D. W. Si/$TiSi_2$ hetero-nanostructures as high-capacity anode material for Li ion batteries. *Nano Lett.* **2010**, *10*, 860–863.

[9] Gu, X.; Chen, L.; Ju, Z. C.; Xu, H. Y.; Yang, J.; Qian, Y. T. Controlled growth of porous α-Fe_2O_3 branches on β-MnO_2 nanorods for excellent performance in lithium-ion batteries. *Adv. Funct. Mater.* **2013**, *23*, 4049–4056.

[10] Milliron, D. J.; Hughes, S. M.; Cui, Y.; Manna, L.; Li, J. B.; Wang, L. W.; Alivisatos, A. P. Colloidal nanocrystal heterostructures with linear and branched topology. *Nature* **2004**, *430*, 190–195.

[11] Xie, X. Q.; Ao, Z. M.; Su, D. W.; Zhang, J. Q.; Wang, G. X. MoS_2/graphene composite anodes with enhanced performance for sodium-ion batteries: The role of the two-dimensional heterointerface. *Adv. Funct. Materi.* **2015**, *25*, 1393–1403.

[12] Bonaccorso, F.; Colombo, L.; Yu, G.; Stoller, M.; Tozzini, V.; Ferrari, A. C.; Ruoff, R. S.; Pellegrini, V. Graphene, related two-dimensional crystals, and hybrid systems for energy conversion and storage. *Science* **2015**, *347*, 1246501.

[13] Peng, L. L.; Peng, X.; Liu, B. R.; Wu, C. Z.; Xie, Y.; Yu, G. H. Ultrathin two-dimensional MnO_2/graphene hybrid nanostructures for high-performance, flexible planar supercapacitors. *Nano Lett.* **2013**, *13*, 2151–2157.

[14] Li, Y. B.; Zhang, J. S.; Zheng, G. Y.; Sun, Y. M.; Hong, S. S.; Xiong, F.; Wang, S.; Lee, H. R.; Cui, Y. Lateral and vertical two-dimensional layered topological insulator heterostructures. *ACS Nano* **2015**, *9*, 10916–10921.

[15] Kang, S. K.; Murphy, R. K. J.; Hwang, S. W.; Lee, S. M.; Harburg, D. V.; Krueger, N. A.; Shin, J.; Gamble, P.; Cheng, H. Y.; Yu, S. et al. Bioresorbable silicon electronic sensors for the brain. *Nature* **2016**, *530*, 71–76.

[16] Xu, L.; Jiang, Z.; Mai, L. Q.; Qing, Q. Multiplexed free-standing nanowire transistor bioprobe for intracellular recording: A general fabrication strategy. *Nano Lett.* **2014**, *14*, 3602−3607.

[17] Xiong, F.; Wang, H. T.; Liu, X. G.; Sun, J.; Brongersma, M.; Pop, E.; Cui, Y. Li intercalation in MoS_2: *In situ* observation of its dynamics and tuning optical and electrical properties. *Nano Lett.* **2015**, *15*, 6777–6784.

[18] Yang, Y.; Xie, C.; Ruffo, R.; Peng, H. L.; Kim, D. K.; Cui, Y. Single nanorod devices for battery diagnostics: A case study on $LiMn_2O_4$. *Nano Lett.* **2009**, *9*, 4109–4114.

[19] Huang, J. Y.; Zhong, L.; Wang, C. M.; Sullivan, J. P.; Xu, W.; Zhang, L. Q.; Mao, S. X.; Hudak, N. S.; Liu, X. H.; Subramanian, A. et al. *In situ* observation of the electrochemical lithiation of a single SnO$_2$ nanowire electrode. *Science* **2010**, *330*, 1515–1520.

[20] Fei, L. F.; Lei, S. J.; Zhang, W. B.; Lu, W.; Lin, Z. Y.; Lam, C. H.; Chai, Y.; Wang, Y. Direct TEM observations of growth mechanisms of two-dimensional MoS$_2$ flakes. *Nat. Commun.* **2016**, *7*, 12206.

[21] Mai, L. Q.; Dong, Y. J.; Xu, L.; Han, C. H. Single nanowire electrochemical devices. *Nano Lett.* **2010**, *10*, 4273–4278.

[22] Hu, P.; Yan, M. Y.; Wang, X. P.; Han, C. H.; He, L.; Wei, X. J.; Niu, C. J.; Zhao, K. N.; Tian, X. C.; Wei, Q. L. et al. Single-nanowire electrochemical probe detection for internally optimized mechanism of porous graphene in electrochemical devices. *Nano Lett.* **2016**, *16*, 1523–1529.

[23] Hong, X. P.; Kim, J.; Shi, S. F.; Zhang, Y.; Jin, C. H.; Sun, Y. H.; Tongay, S.; Wu, J. Q.; Zhang, Y. F.; Wang, F. Ultrafast charge transfer in atomically thin MoS$_2$/WS$_2$ heterostructures. *Nat. Nanotechnil.* **2014**, *9*, 682–686.

[24] Cui, X.; Lee, G. H.; Kim, Y. D.; Arefe, G.; Huang, P. Y.; Lee, C. H.; Chenet, D. A.; Zhang, X.; Wang, L.; Ye, F. et al. Multi-terminal transport measurements of MoS$_2$ using a van der Waals heterostructure device platform. *Nat. Nanotechnol.* **2015**, *10*, 534–540.

[25] Zhou, J. W.; Qin, J.; Zhang, X.; Shi, C. S.; Liu, E. Z.; Li, J. J.; Zhao, N. Q.; He, C. N. 2D space-confined synthesis of few-layer MoS$_2$ anchored on carbon nanosheet for lithium-ion battery anode. *ACS Nano* **2015**, *9*, 3837–3848.

[26] Cao, L. J.; Yang, S. B.; Gao, W.; Liu, Z.; Gong, Y. J.; Ma, L. L.; Shi, G.; Lei, S. D.; Zhang, Y. H.; Zhang, S. T. et al. Direct laser-patterned micro-supercapacitors from paintable MoS$_2$ films. *Small* **2013**, *9*, 2905–2910.

[27] Xiao, J.; Choi, D.; Cosimbescu, L.; Koech, P.; Liu, J.; Lemmon, J. P. Exfoliated MoS$_2$ nanocomposite as an anode material for lithium ion batteries. *Chem. Mater.* **2010**, *22*, 4522–4524.

[28] Zhao, C. Y.; Kong, J. H.; Yao, X. Y.; Tang, X. S.; Dong, Y. L.; Phua, S. L.; Lu, X. H. Thin MoS$_2$ nanoflakes encapsulated in carbon nanofibers as high-performance anodes for lithium-ion batteries. *ACS Appl. Mater. Interfaces* **2014**, *6*, 6392–6398.

[29] Cao, X. H.; Shi, Y. M.; Shi, W. H.; Rui, X. H.; Yan, Q. Y.; Kong, J.; Zhang, H. Preparation of MoS$_2$-coated three-dimensional graphene networks for high-performance anode material in lithium-ion batteries. *Small* **2013**, *9*, 3433–3438.

[30] Chang, K.; Chen, W. X. *In situ* synthesis of MoS$_2$/graphene nanosheet composites with extraordinarily high electro-chemical performance for lithium ion batteries. *Chem.*

Commun. **2011**, *47*, 4252–4254.

[31] Oakes, L.; Carter, R.; Hanken, T.; Cohn, A. P.; Share, K.; Schmidt, B.; Pint, C. L. Interface strain in vertically stacked two-dimensional heterostructured carbon-MoS$_2$ nanosheets controls electrochemical reactivity. *Nat. Commun.* **2016**, *7*, 11796.

[32] Tompsett, D. A.; Islam, M. S. Electrochemistry of hollandite α-MnO$_2$: Li-ion and Na-ion insertion and Li$_2$O incorporation. *Chem. Mater.* **2013**, *25*, 2515–2526.

[33] Ling, C.; Zhang, R. G.; Arthur, T. S.; Mizuno, F. How general is the conversion reaction in Mg battery cathode: A case study of the magnesiation of α-MnO$_2$. *Chem. Mater.* **2015**, *27*, 5799–5807.

[34] Khan, Z.; Park, S.; Hwang, S. M.; Yang, J. C.; Lee, Y.; Song, H.; Kim, Y.; Ko, H. Hierarchical urchin-shaped α-MnO$_2$ on graphene-coated carbon microfibers: A binder-free electrode for rechargeable aqueous Na–air battery. *NPG Asia Mater.* **2016**, *8*, e294.

[35] Shen, X. W.; Qian, T.; Zhou, J. Q.; Xu, N.; Yang, T. Z.; Yan, C. L. Highly flexible full lithium batteries with self-knitted α-MnO$_2$ fabric foam. *ACS Appl. Mater. Interfaces* **2015**, *45*, 25298–25305.

[36] Lu, X. Y.; Deng, J. W.; Si, W. P.; Sun, X. L.; Liu, X. H.; Liu, B.; Liu, L. F.; Oswald, S.; Baunack, S.; Grafe, H. J. et al. High-performance Li-O$_2$ batteries with trilayered Pd/MnO$_x$/Pd nanomembranes. *Adv. Sci.* **2015**, *2*, 1500113.

[37] Lee, Y. H.; Zhang, X. Q.; Zhang, W. J.; Chang, M. T.; Lin, C. T.; Chang, K. D.; Yu, Y. C.; Wang, J. T. W.; Chang, C. S.; Li, L. J. et al. Synthesis of large-area MoS$_2$ atomic layers with chemical vapor deposition. *Adv. Mater.* **2012**, *24*, 2320–2325.

[38] Kwak, J. Y.; Hwang, J.; Calderon, B.; Alsalman, H.; Munoz, N.; Schutter, B.; Spencer, M. G. Electrical characteristics of multilayer MoS$_2$ FET's with MoS$_2$/graphene heterojunction contacts. *Nano Lett.* **2014**, *14*, 4511–4516.

[39] Lee, C. G.; Yan, H. G.; Brus, L. E.; Heinz, T. F.; Hone, J.; Ryu, S. Anomalous lattice vibrations of single-and few-layer MoS$_2$. *ACS Nano* **2010**, *4*, 2695–2700.

[40] Windom, B. C.; Sawyer, W.; Hahn, D. W. A Raman spectroscopic study of MoS$_2$ and MoO$_3$: Applications to tribological systems. *Tribol. Lett.* **2011**, *42*, 301–310.

[41] Gao, T.; Fjellvåg, H.; Norby, P. A comparison study on Raman scattering properties of α- and β-MnO$_2$. *Anal. Chim. Acta* **2009**, *648*, 235–239.

[42] Julien, C. M.; Massot, M.; Poinsignon, C. Lattice vibrations of manganese oxides: Part I. Periodic structures. *Spectrochim. Acta A* **2004**, *60*, 689–700.

[43] Sinha, A. K.; Basu, M.; Pradhan, M.; Sarkar, S.; Negishi, Y.; Pal, T. Thermodynamic and kinetics aspects of spherical

MnO$_2$ nanoparticle synthesis in isoamyl alcohol: An *ex situ* study of particles to one-dimensional shape transformation. *J. Phys. Chem. C* **2010**, *114*, 21173–21183.

[44] Mai, L. Q.; Minhas-Khan, A.; Tian, X. C.; Hercule, K. M.; Zhao, Y. L.; Lin, X.; Xu, X. Synergistic interaction between redox-active electrolyte and binder-free functionalized carbon for ultrahigh supercapacitor performance. *Nat. Commun.* **2013**, *4*, 2923.

[45] Ren, Y.; Ma, Z.; Bruce, P. G. Ordered mesoporous metal oxides: Synthesis and applications. *Chem. Soc. Rev.* **2012**, *41*, 4909–4927.

[46] Brezesinski, T.; Wang, J.; Tolbert, S. H.; Dunn, B. Ordered mesoporous α-MoO$_3$ with iso-oriented nanocrystalline walls for thin-film pseudocapacitors. *Nat. Mater.* **2010**, *9*, 146–151.

[47] Sathiya, M.; Prakash, A.; Ramesha, K.; Tarascon, J. M.; Shukla, A. V$_2$O$_5$-anchored carbon nanotubes for enhanced electrochemical energy storage. *J. Am. Chem. Soc.* **2011**, *133*, 16291–16299.

[48] Rakhi, R. B.; Chen, W.; Cha, D.; Alshareef, H. N. Substrate dependent self-organization of mesoporous cobalt oxide nanowires with remarkable pseudocapacitance. *Nano Lett.* **2012**, *12*, 2559–2567.

[49] Wang, X. P.; Niu, C. J.; Meng, J. S.; Hu, P.; Xu, X. M.; Wei, X. J.; Zhou, L.; Zhao, K. N.; Luo, W.; Yan, M. Y. et al. Novel K$_3$V$_2$(PO$_4$)$_3$/C bundled nanowires as superior sodium-ion battery electrode with ultrahigh cycling stability.

Adv. Energy Mater. **2015**, *5*, 1500716.

[50] Cummins, D. R.; Martinez, U.; Sherehiy, A.; Kappera, R.; Martinez-Garcia, A.; Schulze, R. K.; Jasinski, J.; Zhang, J.; Gupta, R.; Lou, J. et al. Efficient hydrogen evolution in transition metal dichalcogenides via a simple one-step hydrazine reaction. *Nat. Commun.* **2016**, *7*, 11857.

[51] Li, H.; Yin, Z. Y.; He, Q. Y.; Li, H.; Huang, X.; Lu, G.; Fam, D. W. H.; Tok, A. I. Y.; Zhang, Q.; Zhang, H. Fabrication of single- and multilayer MoS$_2$ film-based field-effect transistors for sensing NO at room temperature. *Small* **2012**, *8*, 63–67.

[52] Ruetschi, P. Cation-vacancy model for MnO$_2$. *J. Electrochem. Soc.* **1984**, *131*, 2737–2744.

[53] Ruetschi, P.; Giovanoli, R. Cation vacancies in MnO$_2$ and their influence on electrochemical reactivity. *J. Electrochem. Soc.* **1988**, *135*, 2663–2669.

[54] Ruetschi, P. Influence of cation vacancies on the electrode potential of MnO$_2$. *J. Electrochem. Soc.* **1988**, *135*, 2657–2663.

[55] Bogusz, A.; Bürger, D.; Skorupa, I.; Schmidt, O. G.; Schmidt, H. Bipolar resistive switching in YMnO$_3$/Nb:SrTiO$_3$ PN-heterojunctions. *Nanotechnology* **2016**, *45*, 455201.

[56] Sutar, S.; Agnihotri, P.; Comfort, E.; Taniguchi, T.; Watanabe, K.; Lee, J. U. Reconfigurable p–n junction diodes and the photovoltaic effect in exfoliated MoS$_2$ films. *Appl. Phys. Lett.* **2014**, *104*, 122104.